

Conducting Materials

Two-Dimensional Tetrathiafulvalene Covalent Organic Frameworks: Towards Latticed Conductive Organic Salts

Shangbin Jin,^[a] Tsuneaki Sakurai,^[b] Tim Kowalczyk,^[c] Sasanka Dalapati,^[a] Fei Xu,^[a] Hao Wei,^[a] Xiong Chen,^[a] Jia Gao,^[a] Shu Seki,^[b] Stephan Irle,^[c] and Donglin Jiang^{*[a]}

Abstract: The construction of a new class of covalent TTF lattice by integrating TTF units into two-dimensional covalent organic frameworks (2D COFs) is reported. We explored a general strategy based on the $C_2 + C_2$ topological diagram and applied to the synthesis of microporous and mesoporous TTF COFs. Structural resolutions revealed that both COFs consist of layered lattices with periodic TTF columns and tetragonal open nanochannels. The TTF columns offer predesigned pathways for high-rate hole transport, predominate the HOMO and LUMO levels of the COFs, and are redox active to form organic salts that exhibit enhanced electric conductivity by several orders of magnitude. On the other hand, the linkers between the TTF units play a vital role in determining the carrier mobility and conductivity through the perturbation of 2D sheet conformation and interlayer distance. These results open a way towards designing a new type of TTF materials with stable and predesignable lattice structures for functional exploration.

Tetrathiafulvalene (TTF) is among the most widely utilized molecules for developing molecular metals, whereas the mono-oxidized cation radical of TTF in organic salts presents partially filled band structure and conductivity in the solid state.^[1] However, the solid-state structure of neutral TTF-based molecules is essentially determined by short-range and nondirectional van der Waals forces, which govern the association of TTF molecules and leave an uncontrolled structural formation, as was observed for the polymorph of crystals.^[2] The introduction of

additional interaction sites to the TTF backbone has been proven to be useful for directing the supramolecular assembly of TTF derivatives.^[3] However, it is difficult to use these strategies to crystallize TTF molecules into robust lattice structures. Construction of a latticed TTF structure with predesigned molecular ordering remains a challenge.

Covalent organic frameworks (COFs) are a class of crystalline porous polymers that allow atomically precise integration of organic building blocks into periodic structures.^[4] A significant feature is that the growth pattern of the lattice is solely controlled by the topological design diagram. COFs have emerged as a powerful platform for synthesizing latticed organic structures with predesigned molecular orderings. A variety of π molecules, including arenes, porphyrins, phthalocyanines, thiophenes, and diimides have been explored for the synthesis of COFs, which exhibit remarkable light-emitting, semiconducting, and photoconductive properties.^[4–30] However, the construction of COFs based on TTF, a benchmark electron-donating molecule for organic metals, is unprecedented. Herein, we report the design, structure, and electric functions of TTF COFs (Scheme 1).

TTF assumes a C_2 geometry with four substitutions at second, third, sixth, and seventh positions that form intersection angles substituents defining the COF architecture.^[27] We established a general strategy based on the $C_2 + C_2$ topological diagram for integrating TTF units into COFs. 2,3,6,7-Tetra(4-formylphenyl)-tetrathiafulvalene monomer^[31] and two representative C_2 -symmetric co-monomers, including the simplest disubstituted phenyldiamine and the tetrasubstituted pyrene tetraphenyltetraamine, were used for the synthesis of crystalline microporous and mesoporous COFs (Scheme 1 a, TTF-Ph-COF and TTF-Py-COF). Both COFs consist of lattice structure; however, their TTF textures are different. In TTF-Ph-COF, the TTF units occupy all the vertices of the 2D polygons, whereas in the TTF-Py-COF case, the TTF units only account for half of the vertices (Scheme 1 a). This topological strategy controls the sequence and density of TTF units in the lattice.

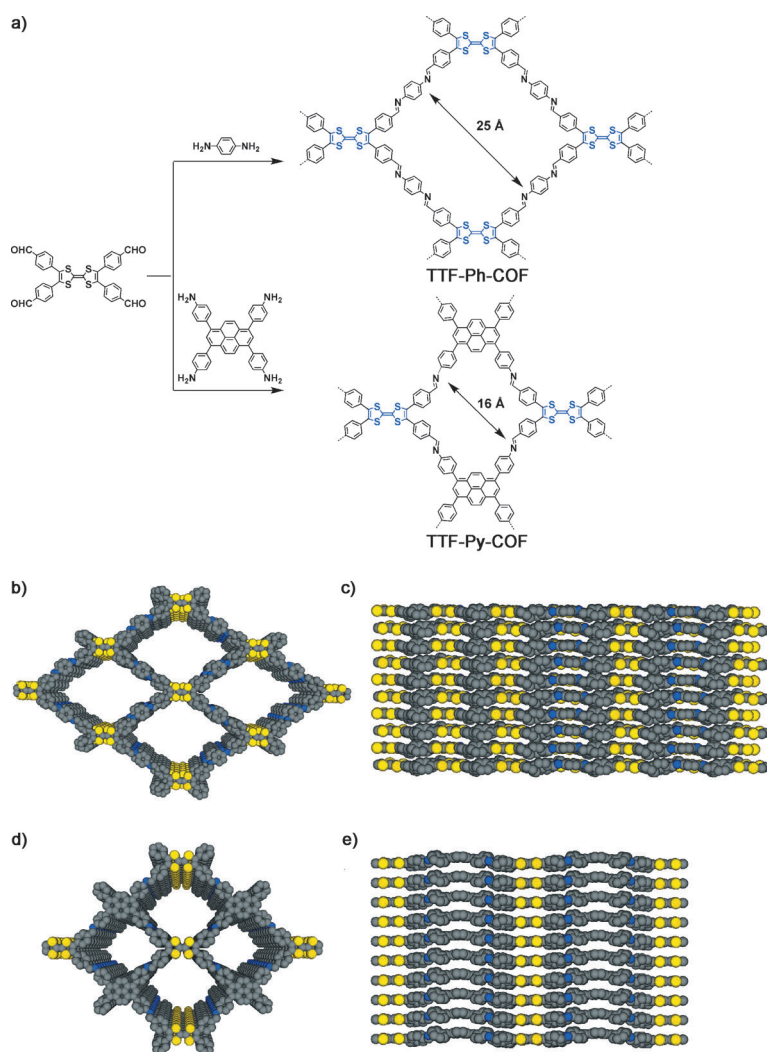
As a typical protocol, a mixture of 2,3,6,7-tetra(4-formylphenyl) tetrathiafulvalene and 1,4-phenyldiamine in dioxane/mesitylene/3 M AcOH (5:5:2 by volume) or a mixture of 2,3,6,7-tetra(4-formylphenyl) tetrathiafulvalene and 1,3,6,8-tetra(4-aminophenyl)pyrene in *n*BuOH/*o*-dichlorobenzene/3 M AcOH (5:5:2 by volume) was sonicated for 1 min, degassed through three freeze/pump/thaw cycles, sealed, and kept at 120 °C. After cooling, the precipitate was collected by centrifugation, washed with $CHCl_3$ and THF, and dried at 100 °C under vacuum

[a] Dr. S. Jin, Dr. S. Dalapati, F. Xu, Prof. Dr. H. Wei, Dr. X. Chen, J. Gao, Prof. Dr. D. Jiang
Department of Materials Molecular Science
Institution for Molecular Science
National Institutes of Natural Sciences
5-1 Higashiyama, Myodaiji, Okazaki 444-8787 (Japan)
E-mail: jiang@ims.ac.jp

[b] Dr. T. Sakurai, Prof. S. Seki
Department of Applied Chemistry, Graduate School of Engineering
Osaka University, 2-1 Yamadaoka, Suita, Osaka 565-0871 (Japan)

[c] Dr. T. Kowalczyk, Prof. S. Irle
World Premier International Research Initiative-Institute of Transformative Bio-Molecules and Department of Chemistry,
Nagoya University, Furo-cho, Chikusa-ku
Nagoya 464-8602 (Japan)

Supporting information for this article is available on the WWW under <http://dx.doi.org/10.1002/chem.201402844>.



Scheme 1. a) Schematic representation of the synthesis of mesoporous TTF-Ph-COF and microporous TTF-Py-COF by a $C_2 + C_2$ topological diagram. Slipped AA stacking structures of TTF-Ph-COF at b) top and c) side views and eclipsed stacking structures of TTF-Py-COF at d) top and e) side views (yellow: S, blue: N, grey: C; H was omitted for clarity).

to give TTF-Ph-COF and TTF-Py-COF as brown and yellowish solids in 55 and 62% isolated yields, respectively (see the Supporting Information). IR spectra of TTF-Ph-COF and TTF-Py-COF confirmed the presence of characteristic C=N vibration bands at $\tilde{\nu} = 1621 \text{ cm}^{-1}$ (Figure S1 in the Supporting Information). Elemental analysis revealed that the C, H, and N contents are close to their theoretical values in infinite 2D sheets (see the Supporting Information). Field-emission scanning electron microscopy images showed plate-like morphology (Figure S2 in the Supporting Information). High-resolution transmission electron microscopy images revealed the porous textures (Figure S2 in the Supporting Information).

To resolve the crystalline structure, we employed a combination of techniques including: 1) Pawley refinement to confirm the XRD peak assignment; 2) density-functional tight-binding (DFTB) calculations to produce the optimal structure of the layered unit cell; and 3) utilization of the optimal unit cell to reconstruct the XRD pattern and to establish the lattice struc-

ture. TTF-Ph-COF and TTF-Py-COF are highly crystalline polymers with strong XRD peaks. TTF-Ph-COF exhibited XRD signals at 3.70 , 7.52 , and 26.0° , which were assignable to the (110) (220), and (001) facets, respectively (Figure 1 a, red curve). Pawley refinement based on a C_2/m monoclinic space group with lattice parameters of $a = 39.964$, $b = 29.267$, $c = 3.89 \text{ \AA}$, and $\alpha = \gamma = 90$, $\beta = 89.24^\circ$ gave an XRD pattern (green curve) that is in good agreement with the experimentally observed pattern, as was evidenced by their negligible difference (black curve). The slipped AA stacking mode (see below) generated an XRD pattern that reproduced the experimentally observed curves (blue curve), whereas the staggered AB mode (purple curve) could not reproduce the XRD pattern and caused overlapped pores (Figure 1 b). On the other hand, TTF-Py-COF displayed XRD peaks at 5.30 , 10.86 , and 23.2 , which can be attributed to the (110), (220), and (001) facets, respectively (Figure 1 c, red curve). Pawley refinement (green curve) TTF-Py-COF based on a C_2/m monoclinic space group with lattice parameters of $a = 36.739$, $b = 20.158$, $c = 3.69 \text{ \AA}$ and $\alpha = \gamma = 90$, $\beta = 89.18^\circ$ reproduces the XRD pattern, confirming the above-described peak assignment. XRD pattern simulations by using the eclipsed AA stacking mode (blue curve) reproduced the experimental profile, whereas the staggered AB stacking mode (purple curve) failed to reproduce the XRD pattern and gave rise to overlapped pores (Figure 1 d).

In the case of TTF-Py-COF, there are two potential structures in terms of different orientation of pyrene and TTF units. TTF-Py-COF with the parallel alignment of pyrene and TTF units is named as α -TTF-Py-COF, whereas the one with the perpendicular alignment of pyrene and TTF units is denoted as β -TTF-Py-COF. However, β -TTF-Py-COF has two different pore sizes and give completely different XRD pattern from the experimentally observed one (Figure S3 in the Supporting Information). Therefore, TTF-Py-COF is in the form of α -TTF-Py-COF, whereas the pyrene units are parallel oriented (Scheme 1 d and e). We employed the self-consistent charge-density functional tight-binding method (SCC-DFTB) with empirical Lennard-Jones dispersion for calculating optimal crystal structures (see the Support-

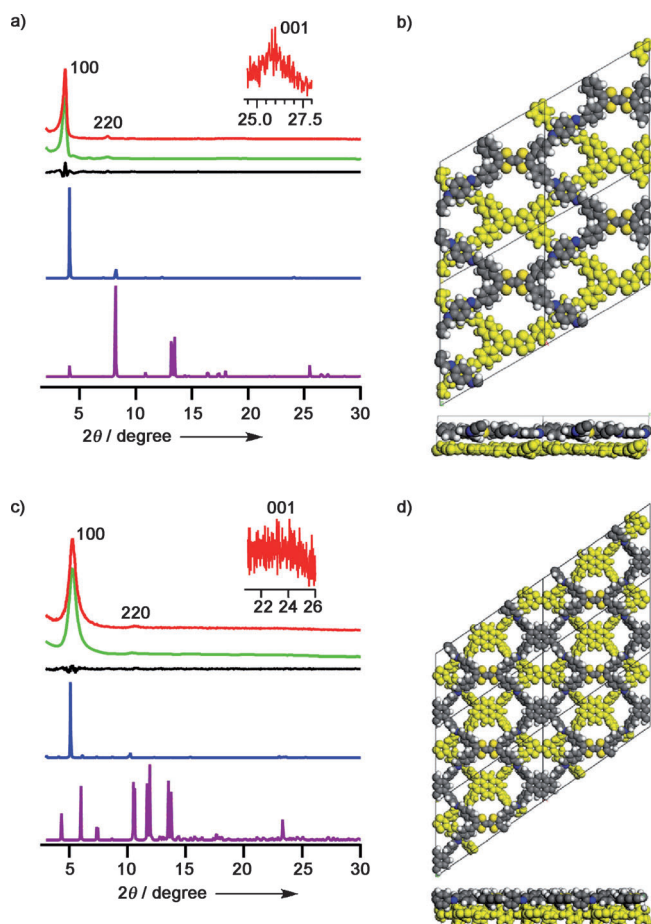


Figure 1. XRD patterns of a) TTF-Ph-COF and c) TTF-Py-COF (red: observed curve, green: Pawley refined curve, black: their difference, blue: Slipped AA stacking mode or eclipsed AA stacking mode, purple: staggered AB mode). Stacking structure of the staggered AB modes of b) TTF-Ph-COF and d) TTF-Py-COF (top and side views).

ing Information). The structure of the TTF-Ph-COF monolayer was first determined by using a hexagonal unit cell to define the periodic boundary; however, a monoclinic unit cell was required for TTF-Py-COF as its geometry requires unequal lattice vector lengths $a \neq b$. TTF-Ph-COF and TTF-Py-COF monolayers have unit-cell lattice parameters of $a = 24.8$, $b = 24.9$ and $a = 36.1$, $b = 20.8$ Å, respectively. Based on these optimal monolayer structures, three stacking lattices, including eclipsed AA, slipped AA, and staggered AB modes, were calculated.

We set an initial slip distance of 0.8 Å along the a and b directions for the slipped AA stacking structure and found that these values converge at 0.35 Å. Of the three modes, TTF-Ph-COF preferred a slipped AA stacking mode (Scheme 1 b and c; Table 1). This slipped stacking mode gains a total crystal stacking energy of 56.7 kcal mol⁻¹ per unit cell. On the other hand, the eclipsed AA stacking mode gives rise to a lower total crystal stacking energy of 51.4 kcal mol⁻¹. For the staggered AB stacking mode, the total

crystal stacking energy decreased to 46.5 kcal mol⁻¹, as a result of losing π - π forces between 2D layers.

TTF-Py-COF adopts the eclipsed AA stacking mode (Scheme 1 d,e) among the different geometries (Table 1). Compared with TTF-Ph-COF, the total crystal-stacking energy of TTF-Py-COF is enhanced to 84.8 and 82.4 kcal mol⁻¹ for the eclipsed and slipped AA stacking modes, respectively (Table 1), indicating that the large pyrene π linker that occupies the vertices of TTF-Py-COF does contribute to the interlayer stacking forces, in addition to the TTF interactions. On the other hand, the eclipsed AB (Figure S3 in the Supporting Information) and staggered AB modes exhibited severely reduction of stacking energy to only 69.2 and 47.0 kcal mol⁻¹, respectively (Table 1). The low total stacking energy of the eclipsed AB stacking mode also supports that TTF-Py-COF favors the eclipsed AA stacking structure.

The above-described results indicate that both TTF COFs constitute periodic TTF columns and ordered porous channels, as shown in Scheme 1 b–e. A closer examination of the interlayer structures revealed that their interlayer distance is different. TTF-Ph-COF has an interlayer distance of 3.71 Å for the slipped AA stacking mode, whereas TTF-Py-COF adopts a longer distance of 3.87 Å (Table 1). Meanwhile, TTF-Ph-COF assumes an almost planar sheet conformation, whereas TTF-Py-COF display a distorted conformation (Scheme 1 c,e). These differences in layered structures originate from the difference of linkers between TTF units in the COFs. The phenyl linker in TTF-Ph-COF has a planar conformation, whereas the paddle-shaped tetraphenylpyrene linker distorts the 2D layer from a planar conformation and expands the interlayer distance. Therefore, the linker in the COFs not only tunes the periodicity of the TTF columns but also perturbs the conformation of 2D layers and their interlayer distance, which are the key to electric functions, such as carrier transport and conductivity. Because the imine linkage extends π conjugation of the TTF cores, how the imine linkage and linker unit affect the HOMO and LUMO levels of the TTF units is an important consideration in the formation of charge transfer complexes. In the monolayer, the HOMO–LUMO pair centers on the TTF units in both COFs, with some delocalized π bonding over the adjacent linkers (Figure S4 in the Supporting Information). These frontier MOs have negligible weight on the pyrene cores in TTF-Py-

Table 1. DFTB calculation results on the lattice vector length c value, total crystal-stacking energy per unit cell (E_{total}), and HOMO–LUMO levels.

COFs	Mode	c [Å]	$E_{\text{dispersion}}$ [kcal mol ⁻¹]	E_{total} [kcal mol ⁻¹]	HOMO/LUMO [eV]
TTF-Ph-COF	monolayer	–	291.8	–	–4.60/–3.31
	eclipsed AA	3.83	473.7	51.4	–4.30/–3.50
	slipped AA	3.71	473.5	56.7	–4.35/–3.51
	staggered AB	3.46	491.4	46.5	–4.53/–3.58
TTF-Py-COF	monolayer	–	448.8	–	–4.61/–3.24
	eclipsed AA	3.87	731.7	84.8	–4.39/–3.61
	slipped AA	3.83	736.1	82.4	–4.51/–3.58
	staggered AB	3.92	817.0	47.0	–4.85/–3.66
	eclipsed AB	4.02	757.0	69.2	–4.54/–3.49

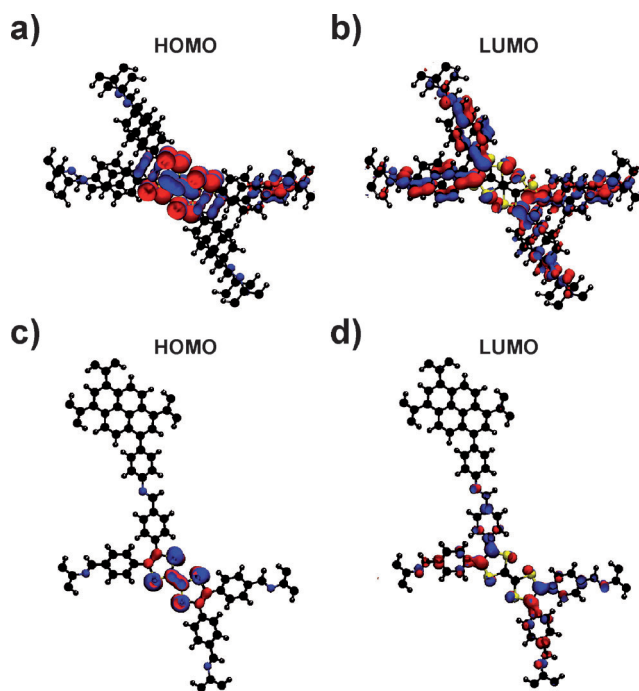


Figure 2. HOMO and LUMO of (a, b) the slipped-AA stacking TTF-Ph-COF and (c, d) the eclipsed AA stacking TTF-Py-COF.

COF. In both COFs, the HOMO includes the C=C π bond across the TTF unit, whereas this C=C unit is merely nonbonding (not anti-bonding) in the LUMO. In the optimized layer lattices, the stacking only perturbs the frontier orbitals (Figures 2 and S4 in the Supporting Information); they remain qualitatively the same as their counterparts in the monolayer. These results suggest that the HOMO and LUMO levels (Table 1) and redox activity (see below) of the COFs are dominated by the TTF units, with less interference by the phenyl and pyrene linkers.

Thermal gravimetric analysis revealed that TTF-Ph-COF and TTF-Py-COF have no obvious weight loss until 450 °C (Figure S5 in the Supporting Information). The chemical stability in different solvents was investigated (Figure 3). The COFs are stable in hexane, methanol, water, and alkaline solution (aqueous 1 M NaOH solution).

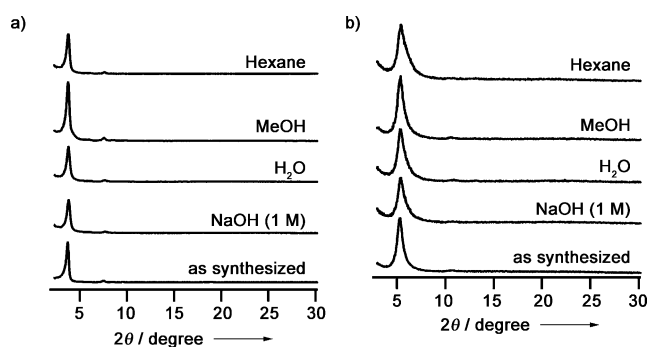


Figure 3. XRD patterns of a) TTF-Ph-COF and b) TTF-Py-COF upon one-day treatment in different conditions.

Nitrogen-sorption-isotherm measurements were conducted at 77 K. TTF-Ph-COF exhibited a reversible sorption curve with Brunauer–Emmett–Teller (BET) surface area as high as 1014 m²g⁻¹ and pore volume of 1.22 cm³g⁻¹ (Figure 4a). The pore-size distribution profile obtained by using nonlocal density functional theory (NLDFT) method revealed that TTF-Ph-COF

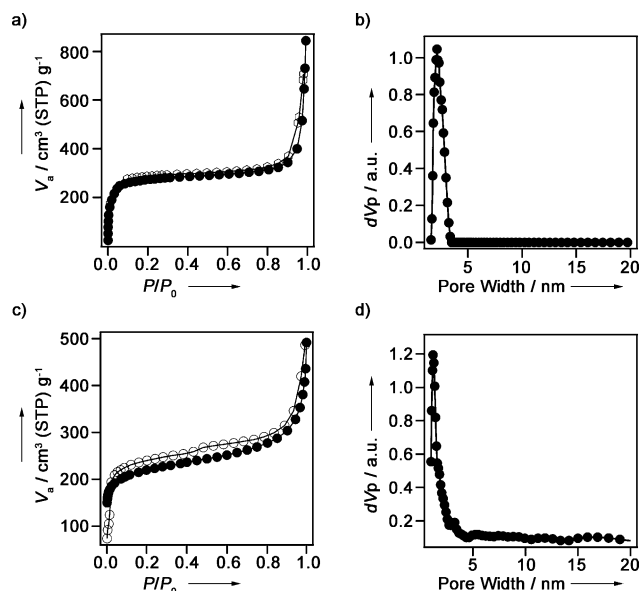


Figure 4. Nitrogen sorption isotherm curves of a) TTF-Ph-COF and c) TTF-Py-COF (filled circle: adsorption, open circle: desorption) at 77 K. Pore size distribution of b) TTF-Ph-COF and d) TTF-Py-COF using the NLDFT method.

consists of one type of mesopore with size of 2.2 nm, which accounts for the porosity (Figure 4b). On the other hand, TTF-Py-COF has a BET surface area of 817 m²g⁻¹ and pore volume of 0.76 cm³g⁻¹ (Figure 4c). The pore-size distribution curve confirmed the presence of only one kind of micropore with size of 1.3 nm (Figure 4d).

TTF is a typical hole-transporting compound. To reveal the conducting properties of the COFs with periodically aligned TTF columns, we utilized the electrodeless flash-photolysis time-resolved microwave conductivity (FP-TRMC) method, which measures the inherent charge-carrier mobility within several nanometers after laser pulse irradiation.^[19,32] The excitation of TTF-Ph-COF by a 355 nm pulsed laser at a photon density of 9.1×10^{15} photon cm⁻² gave a maximum $\varphi \Sigma \mu$ value (in which φ is the photocarrier-generation yield and $\Sigma \mu$ is the sum of the mobilities of charge carriers) of $1.1 (\pm 0.05) \times 10^{-5}$ cm²V⁻¹s⁻¹ (Figure 5a). In contrast, TTF-Py-COF (blue curve) gave a $\varphi \Sigma \mu$ value of $5.0 (\pm 0.1) \times 10^{-6}$ cm²V⁻¹s⁻¹, which is half that of TTF-Ph-COF (Figure 5c).

The φ values were determined by using a direct current-integration method (Figure 5b and d and Figure S6 in the Supporting Information). The COF samples were exposed to a 355 nm laser pulse at 9.0×10^{15} photons cm⁻² and the φ values of TTF-Ph-COF and TTF-Py-COF were evaluated to be 5.8×10^{-5} and 6.4×10^{-5} , respectively, by using poly(9,9'-dioctylfluorene) (PDOF) film as a reference. Therefore, the carrier mo-

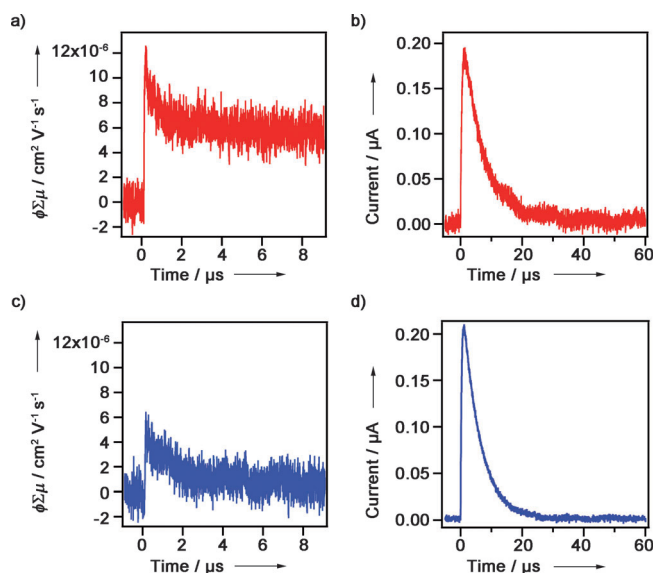


Figure 5. FP-TRMC profiles of a) TTF-Ph-COF and c) TTF-Py-COF. Current of b) TTF-Ph-COF and d) TTF-Py-COF measured by a direct integration method.

bility of TTF-Ph-COF and TTF-Py-COF was 0.2 and $0.08 \text{ cm}^2 \text{ V}^{-1} \text{ s}^{-1}$, respectively. The high carrier mobility observed for TTF-Ph-COF is likely related to its tighter stacking layer structure, as was revealed by the crystalline structure. TTF-COFs consist of high crystalline π columns that provide pre-designed pathways for carrier transport.^[3] The mobilities of these TTF COFs are rather high, in comparison with the crystals of TTF derivatives that have mobilities of 10^{-5} to $1 \text{ cm}^2 \text{ V}^{-1} \text{ s}^{-1}$ with a majority under $10^{-2} \text{ cm}^2 \text{ V}^{-1} \text{ s}^{-1}$.^[35]

The COFs undergo reversible electrochemical reactions. TTF-Ph-COF in acetonitrile exhibited a reversible cyclic voltammetric profile and two clear oxidation peaks at 0.21 and 0.54 V (vs. SCE, Figure S6 in the Supporting Information), which are very close to those (0.21 and 0.53 V) of the monomer (Figure S7 in the Supporting Information). This is also the case for TTF-Py-COF that exhibited two oxidation peaks at 0.22 and 0.55 V. These results are consistent with the HOMO and LUMO mappings and again indicate that the TTF columns in the COFs retain their redox activities. It is known that iodine acts as a suitable oxidant, because it has reduction potentials at 0.615 V (for I^-) and 0.784 V (for I_3^-).^[33] We exemplified this potential by using iodine as an oxidant, because it has been widely utilized for the oxidation of TTF derivatives. Indeed, exposure of the COF samples to iodine vapor caused a quick color change to black, as a result of the formation of a charge-transfer complex. Electronic absorption spectra revealed the drastic enhancement of absorption in the near infrared region 800–1100 nm (Figure S8 in the Supporting Information), which is characteristic of a TTF radical cation and iodide radical-anion pair.^[34] The COF samples upon oxidation retained their original XRD patterns, indicating that their lattice structures remained intact (Figure S9 in the Supporting Information). We pressed COF samples to make tapes with a gap of 0.2 cm, width of 0.4 cm, and thickness of around 0.05 cm for the conductivity measurements (see the Supporting Information). The TTF-Ph-

COF and TTF-Py-COF tapes at 1.0 V bias generate currents of only 2.6×10^{-12} and 2.0×10^{-12} A, respectively (Figure 6a and c, black curves). Upon iodine oxidation, the I - V curves of TTF-Ph-COF and TTF-Py-COF exhibited linear plots, which are characteristics of ohmic conduction (Figure 6a,c, red and blue curves). Time-dependent current profiles revealed that TTF-Ph-

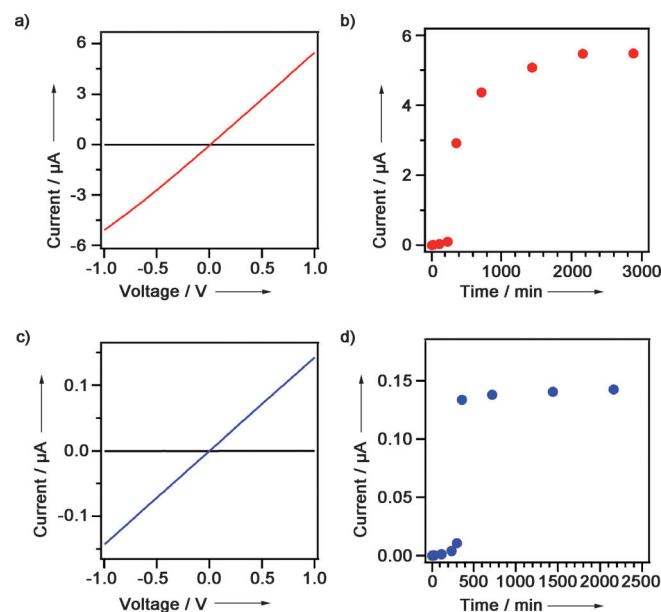


Figure 6. I - V curves of a) TTF-Ph-COF and c) TTF-Py-COF (black curves: pristine COFs, red and blue curves: COFs upon iodine oxidation). Time-dependent current of b) TTF-Ph-COF and d) TTF-Py-COF upon iodine oxidation.

COF reaches the maximal current of 5.5×10^{-6} A upon 36 h oxidation (Figure 6b); the current was enhanced by 10^6 fold. In contrast, TTF-Py-COF exhibited similar oxidation process and required 6 h to reach the maximum current of 1.4×10^{-7} A (Figure 6d); the current was increased by a factor of 10^5 fold. The conductivities of TTF-Ph-COF and TTF-Py-COF were estimated to be 10^{-5} and $10^{-6} \Omega^{-1} \text{ cm}^{-1}$, respectively. Therefore, the latticed TTF columns in the COFs allow the generation of charge-transfer complexes that greatly enhance the electric conductivity, whereas the degree of enhancement is likely related to the layer conformation and interlayer distance perturbed by the linker nature.

In summary, we reported the synthesis, structure, and electric properties of a new class of electric COFs with latticed TTF structures. We established a general topological diagram for the design and synthesis of mesoporous and microporous COFs that are highly crystalline and possess large porosity. The layered structures constitute periodically aligned TTF π columns for high-rate carrier transport and enhanced electric conduction upon oxidation, whereas the linker units play an important role in perturbing the layered lattice and thus the conductivity. This work constitutes a great step towards organic metals with pre-designable lattice architectures.

Acknowledgements

This work was supported by a Grant-in-Aid for Scientific Research (A) (24245030) from MEXT, Japan (D.J.). S.D. thanks IMS fellowship. T.S. and T.K. thank JSPS Fellowship.

Keywords: carrier mobility • conducting materials • covalent organic frameworks • synthetic methods • tetrathiafulvalene

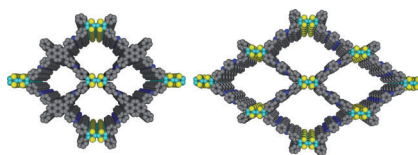
- [1] a) A. Kobayashi, E. Fujiwara, H. Kobayashi, *Chem. Rev.* **2004**, *104*, 5243–5264; b) U. Geiser, J. A. Schlueter, *Chem. Rev.* **2004**, *104*, 5203–5242; c) R. P. Shibaeva, E. B. Yagubskii, *Chem. Rev.* **2004**, *104*, 5347–5378; d) J. L. Segura, N. Martin, *Angew. Chem.* **2001**, *113*, 1416–1455; *Angew. Chem. Int. Ed.* **2001**, *40*, 1372–1409.
- [2] a) M. Mas-Torrent, M. Durkut, P. Hadley, X. Ribas, C. Rovira, *J. Am. Chem. Soc.* **2004**, *126*, 984–985; b) M. Mas-Torrent, P. Hadley, S. T. Bromley, X. Ribas, J. Tarres, M. Mas, E. Molins, J. Veciana, C. Rovira, *J. Am. Chem. Soc.* **2004**, *126*, 8546–8553; c) N. M. Tucker, A. L. Briseno, O. Acton, H. Yip, H. Ma, S. A. Jenekhe, Y. Xia, A. K. Jen, *ACS Appl. Mater. Interfaces* **2013**, *5*, 2320–2324.
- [3] a) I. C. Pintre, J. L. Serrano, M. B. Ros, J. Ortega, I. Alonso, J. Martinez-Perdiguero, C. L. Folcia, J. Etxebarria, F. Goc, D. B. Amabilino, J. Puigmartí-Luis, E. Gomar-Nadal, *Chem. Commun.* **2008**, 2523–2525; b) C. Wang, D. Zhang, D. Zhu, *J. Am. Chem. Soc.* **2005**, *127*, 16372–16373; c) P. Miskiewicz, M. Mas-Torrent, J. Jung, S. Kotarba, I. Glowacki, E. Gomar-Nadal, D. B. Amabilino, J. Veciana, B. Krause, D. Carbone, C. Rovira, J. Ullanski, *Chem. Mater.* **2006**, *18*, 4724–4729.
- [4] X. Feng, X. Ding, D. Jiang, *Chem. Soc. Rev.* **2012**, *41*, 6010–6022.
- [5] A. P. Côté, A. Benin, N. Ockwig, M. O’Keeffe, A. Matzger, O. M. Yaghi, *Science* **2005**, *310*, 1166–1170.
- [6] R. W. Tilford, W. R. Gemmil, H. C. zur Loye, J. J. Lavigne, *Chem. Mater.* **2006**, *18*, 5296–5301.
- [7] H. M. El-Kaderi, J. R. Hunt, J. L. Mendoza-Cortes, A. P. Côté, R. E. Taylor, M. O’Keeffe, O. M. Yaghi, *Science* **2007**, *316*, 268–272.
- [8] A. P. Côté, H. M. El-Kaderi, H. Furukawa, J. R. Hunt, O. M. Yaghi, *J. Am. Chem. Soc.* **2007**, *129*, 12914–12915.
- [9] J. R. Hunt, C. J. Doonan, J. D. LeVangie, A. P. Côté, O. M. Yaghi, *J. Am. Chem. Soc.* **2008**, *130*, 11872–11873.
- [10] R. W. Tilford, S. J. Mugavero, R. J. Pellechia, J. J. Lavigne, *Adv. Mater.* **2008**, *20*, 2741–2746.
- [11] P. Kuhn, M. Antonietti, A. Thomas, *Angew. Chem.* **2008**, *120*, 3499–3502; *Angew. Chem. Int. Ed.* **2008**, *47*, 3450–3453.
- [12] S. Wan, J. Guo, J. Kim, H. Ihee, D. Jiang, *Angew. Chem.* **2008**, *120*, 8958–8962; *Angew. Chem. Int. Ed.* **2008**, *47*, 8826–8830.
- [13] S. Wan, J. Guo, J. Kim, H. Ihee, D. Jiang, *Angew. Chem.* **2009**, *121*, 5547–5550; *Angew. Chem. Int. Ed.* **2009**, *48*, 5439–5442.
- [14] F. J. Uribe-Romo, J. R. Hunt, H. Furukawa, C. Klöck, M. O’Keeffe, O. M. Yaghi, *J. Am. Chem. Soc.* **2009**, *131*, 4570–4571.
- [15] H. Furukawa, O. M. Yaghi, *J. Am. Chem. Soc.* **2009**, *131*, 8875–8883.
- [16] E. L. Spitler, W. R. Dichtel, *Nat. Chem.* **2010**, *2*, 672–677.
- [17] J. W. Colson, A. R. Woll, A. Mukherjee, M. P. Levendorf, E. L. Spitler, V. B. Shields, M. G. Spencer, J. Park, W. R. Dichtel, *Science* **2011**, *332*, 228–231.
- [18] F. J. Uribe-Romo, C. J. Doonan, H. Furukawa, K. Oisaki, O. M. Yaghi, *J. Am. Chem. Soc.* **2011**, *133*, 11478–11481.
- [19] X. Ding, J. Guo, X. Feng, Y. Honsho, J. Guo, S. Seki, P. Maitarad, A. Saeki, S. Nagase, D. Jiang, *Angew. Chem.* **2011**, *123*, 1325–1329; *Angew. Chem. Int. Ed.* **2011**, *50*, 1289–1293.
- [20] M. Dogru, A. Sonnauer, A. Gavryushin, P. Knochel, T. Bein, *Chem. Commun.* **2011**, *47*, 1707–1709.
- [21] K. T. Jackson, T. E. Reich, H. M. El-Kaderi, *Chem. Commun.* **2012**, *48*, 8823–8825.
- [22] S. Jin, X. Ding, X. Feng, M. Supur, K. Furukawa, S. Takahashi, M. Addicoat, M. El-Khouly, T. Nakamura, S. Irle, S. Fukuzumi, A. Nagai, D. Jiang, *Angew. Chem.* **2013**, *125*, 2071–2075; *Angew. Chem. Int. Ed.* **2013**, *52*, 2017–2021.
- [23] S. Jin, K. Furukawa, M. Addicoat, L. Chen, S. Takahashi, S. Irle, T. Nakamura, D. Jiang, *Chem. Sci.* **2013**, *4*, 4505–4511.
- [24] H. Xu, X. Chen, J. Gao, J. Lin, M. Addicoat, S. Irle, D. Jiang, *Chem. Commun.* **2013**, *50*, 1292–1294.
- [25] S. Dalapati, S. Jin, J. Gao, Y. Xu, A. Nagai, D. Jiang, *J. Am. Chem. Soc.* **2013**, *135*, 17310–17313.
- [26] A. Nagai, X. Chen, X. Feng, X. Ding, Z. Guo, D. Jiang, *Angew. Chem.* **2013**, *125*, 3858–3862; *Angew. Chem. Int. Ed.* **2013**, *52*, 3770–3774.
- [27] X. Chen, M. Addicoat, S. Irle, A. Nagai, D. Jiang, *J. Am. Chem. Soc.* **2013**, *135*, 546–549.
- [28] J. Guo, Y. Xu, S. Jin, L. Chen, T. Kaji, Y. Honsho, M. Addicoat, J. Kim, A. Saeki, H. Ihee, S. Seki, S. Irle, M. Hiramoto, J. Gao, D. Jiang, *Nat. Commun.* **2013**, *4*, 2736.
- [29] M. G. Rabbani, A. K. Sekizkardes, Z. Kahveci, T. E. Reich, R. Ding, H. M. El-Kaderi, *Chem. Eur. J.* **2013**, *19*, 3324–3328.
- [30] a) S. Kandambeth, D. Shinde, M. Panda, B. Lukose, T. Heine, R. Banerjee, *Angew. Chem.* **2013**, *125*, 13290–13294; *Angew. Chem. Int. Ed.* **2013**, *52*, 13052–13056; b) B. Biswal, S. Chandra, S. Kandambeth, B. Lukose, T. Heine, R. Banerjee, *J. Am. Chem. Soc.* **2013**, *135*, 5328–5331; c) S. Chandra, S. Kandambeth, B. Biswal, B. Lukose, S. Kunjir, M. Chaudhary, R. Barbarao, T. Heine, R. Banerjee, *J. Am. Chem. Soc.* **2013**, *135*, 17853–17861.
- [31] Y. Mitamura, H. Yorimitsu, K. Oshima, A. Osuka, *Chem. Sci.* **2011**, *2*, 2017–2021.
- [32] A. Saeki, Y. Koizumi, T. Aida, S. Seki, *Acc. Chem. Res.* **2012**, *45*, 1193–1202.
- [33] P. H. Qi, J. B. Hiskey, *Hydrometallurgy* **1993**, *32*, 161–179.
- [34] J. B. Torrance, B. A. Scott, B. Welber, F. B. Kaufman, P. E. Seiden, *Phys. Rev. B* **1979**, *19*, 730–741.
- [35] V. Coropceanu, J. Cornil, D. A. da Silva Filho, Y. Olivier, R. Silbey, J.-L. Bredas, *Chem. Rev.* **2007**, *107*, 926–952.

Received: March 31, 2014

Published online on ■ ■ ■ ■, 0000

COMMUNICATION

Stack in a crystal: The construction of a new class of covalent tetrathiafulvalene (TTF) lattice by integrating TTF units into two-dimensional covalent organic frameworks (2D COFs) is reported (see figure). The linkers between the TTF units play a vital role in determining the carrier mobility and conductivity.

**Conducting Materials**

*S. Jin, T. Sakurai, T. Kowalczyk,
S. Dalapati, F. Xu, H. Wei, X. Chen, J. Gao,
S. Seki, S. Irle, D. Jiang**

■■ – ■■

**Two-Dimensional Tetrathiafulvalene
Covalent Organic Frameworks:
Towards Latticed Conductive Organic
Salts**



Ordered tetrathiafulvalene structures...are constructed by integrating into the lattice of 2D covalent organic frameworks. The tetrathiafulvalene columnar π -arrays offer pathways for high-rate hole transport, determine the frontier orbit levels, and upon oxidation form organic salts that exhibit drastically improved electric conductivity by several orders of magnitude. For more details, see the Communication by D. Jiang et al. on page ■■ ff.